ARTICLE

Control of Particle Size of Pt and Pt Alloy Electrocatalysts Supported on Carbon Black by the Nanocapsule Method

Kazuki Okaya,[†] Hiroshi Yano,[†] Hiroyuki Uchida,[†,§] and Masahiro Watanabe*[,†]

Interdisciplinary Graduate School of Medicine and Engineering, Fuel Cell Nanomaterials Center, and Clean Energy Research Center, University of Yamanashi, Takeda 4, Kofu 400-8510, Japan

ABSTRACT Monodisperse Pt and Pt−M (M = Co, Ru) alloy nanoparticles supported on carbon black (Pt/CB, Pt_2Ru_3/CB, Pt_3Co/CB) were prepared by the nanocapsule method. We have succeeded in controlling the particle size simply by changing the molar ratio of metal precursor(s) to surfactant (M/S) in the preparation, with the other conditions being identical. The particle size was well-controlled between 2.0 and 4.5 nm with a metal loading level of 50 wt % for all catalysts. The compositions of the alloy particles were close to the projected values, with a small standard deviation, i.e., <3.1 atom % for Pt_2Ru_3 and 1.4 atom % for Pt_3Co. It was also found that these alloys were in the form of the corresponding solid solutions with the fcc structure.

KEYWORDS: electrocatalyst • PEFC • Pt • Pt alloy • particle size

INTRODUCTION

Polymer electrolyte fuel cells (PEFCs) have been intensively developed as a primary power source for electric vehicles and residential cogeneration systems. Both the anodes and cathodes of PEFCs, however, usually require costly platinum or its alloys as the catalyst, having a high activity at low operating temperatures <100 °C. For the large-scale commercialization of PEFCs, it is very important to reduce the amount of platinum catalyst used while maintaining the durability.

The cathode catalyst must exhibit high activity for the oxygen reduction reaction (ORR). It has been reported for planar electrodes in acid electrolyte solutions that the ORR activities were enhanced at Pt alloyed with nonprecious metals such as Fe (1–4), Co (1, 4–8), Ni (1, 3–11), Mn (4), Cr (5–7, 12, 13), and V (14).

Regarding the anode reaction in PEFCs, the overpotential for the hydrogen oxidation reaction (HOR) at the Pt anode is negligibly small when pure hydrogen is used as the fuel gas. In contrast, the Pt anode operating with reformates is seriously poisoned by trace amounts of carbon monoxide; CO molecules strongly adsorb on the active sites, blocking the HOR. Thus, the development of CO-tolerant anode catalysts is important, particularly for use in residential cogeneration systems. Among various anode catalysts developed, Pt−Ru alloys are still the best candidates; these exhibit both high CO-tolerance and acceptable durability under practical operating conditions.

To obtain high mass activity for Pt in PEFCs, it is essential to disperse the Pt or Pt alloy nanoparticles described above on high surface area supports such as carbon black (CB). Various binary (4–6, 11, 14–21) and ternary (13, 19, 20, 22, 23) Pt-based alloys supported on CB have been prepared. Often, significant discrepancies have been observed between the properties of nominally similar materials. Because the activities for the ORR and the HOR (or CO tolerances) of these supported Pt-alloy catalysts are not always consistent with those evaluated for bulk alloys, one of the possible reasons could be nonuniform chemical composition within given batches of alloy nanoparticles. For example, in the past, Pt-based alloy/CB catalysts have been prepared by the impregnation of the second metal precursors on Pt/CB, followed by heating at temperatures above 700 °C under inert gas or hydrogen to form the alloys (6, 13, 19–21). However, in the latter reports, such heat treatments frequently caused the agglomeration of the particles, as well as nonuniform composition, depending on the particle size, resulting in a decrease in the mass activity and/or in accelerated degradation of the activity with operation time. By reducing the reaction temperature to around 200 °C with the use of the carbonyl complex process (11) or the water-in-oil microemulsion method, the agglomeration of the alloy particles was suppressed (15), but the control of the alloy composition was still difficult. The average particle size obtained by the conventional colloid method (17, 24–26) was usually large, and the size distribution was also broad.

Assuming the area-specific activity to be independent of the particle size (27), the mass activity of the catalyst increases inversely proportionally to the particle size. In contrast, very small particles (<2 nm) tend to agglomerate or corrode noticeably under practical operating conditions.

* Corresponding author. Phone: +81-55-220-8620. Fax: +81-55-254-0371. E-mail: m-watanabe@yamanashi.ac.jp.

Received for review December 8, 2009 and accepted February 8, 2010

[†] Interdisciplinary Graduate School of Medicine and Engineering, University of Yamanashi.

[‡] Fuel Cell Nanomaterials Center, University of Yamanashi.

[§] Clean Energy Research Center, University of Yamanashi.

DOI: 10.1021/am9008693

Published on Web 02/16/2010

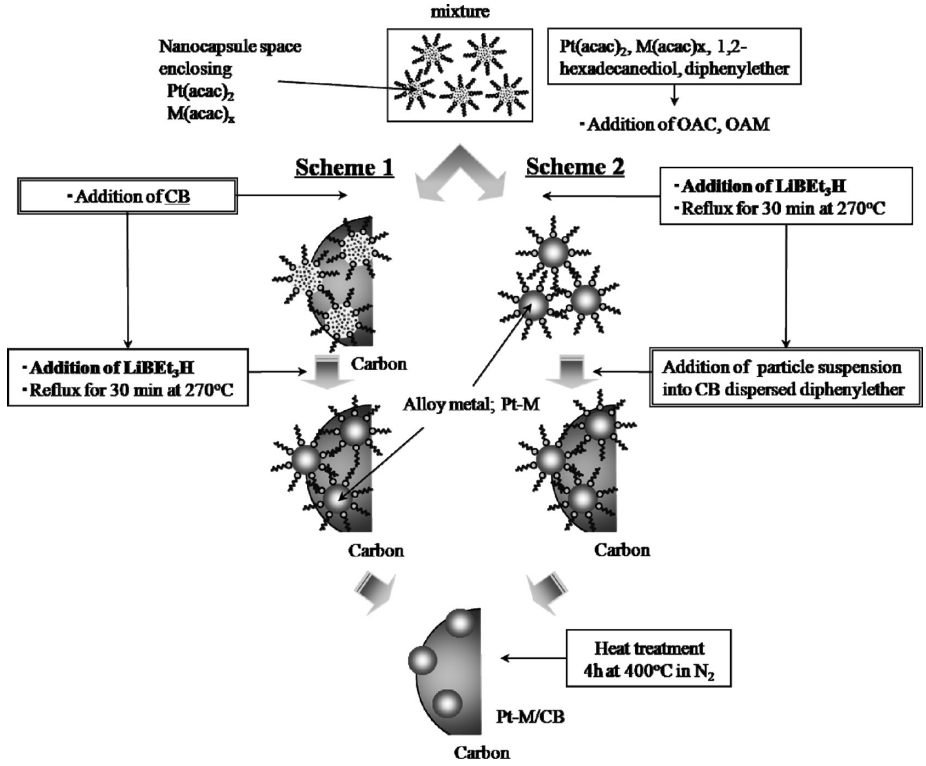

FIGURE 1. Illustration of the preparation protocol for Pt/CB and Pt-M/CB catalysts.

Thus, it is highly desirable to determine the appropriate particle size of Pt-alloys for achieving both high mass activity and high durability. However, as described above, nonuniform chemical composition among the alloy nanoparticles and their broad size distribution are major impediments to progress in the development of alloy electrocatalysts. Hence, it is very important to control the alloy composition uniformly among the entire batch of supported nanoparticles, while maintaining the particle size in a narrow range (monodisperse state).

Recently, there has been great progress in the synthesis of monodisperse Pt−Fe-based alloy nanoparticles for permanent magnetic materials via the simultaneous reduction of platinum(II) acethylacetonate, $Pt(acac)_2$ and $FeCl_2$, and/or cobalt acetylacetonate $Co(acac)_3$ in reverse micelles. The use of such nanocapsules as highly confined reaction chambers should provide monodisperse alloy particles with uniform composition. Liu et al. examined this method for the preparation of anode catalysts for direct methanol fuel cells (DMFCs) (28, 29), where Pt or Pt−Ru alloy particles in nanocapsules were once precipitated by removing the organic moieties consisting of the capsules, followed by the addition of the CB powder support. However, we found in careful inspections that such naked particles without any protection by the organic moieties were partially aggregated on the CB. Therefore, we developed the "nanocapsule method", in which metal precursor(s) within reverse micelles (nanocapsules) were reduced in diphenyl ether in the presence of CB as the support. We succeeded in preparing monodisperse Pt/CB and Pt-M/CB (M = V, Ni, Cr, Co, and Fe) with very uniform alloy compositions, and demonstrated their enhanced ORR activities (30).

In the present research, we examined ways to control the particle size of Pt and Pt−M alloys (M = Ru and Co) supported on CB while maintaining the monodisperse state and uniform composition among entire batches of particles. We have succeeded in controlling the particle size of Pt, Pt−Ru, and Pt−Co alloys in monodisperse state simply by changing the molar ratio of metal precursor(s) to surfactant (M/S) in a modified nanocapsule method. These catalysts were characterized by X-ray diffraction (XRD), scanning transmission electron microscopy (STEM), and energy-dispersive X-ray microanalysis (EDX). The compositions of the alloy particles were found to be close to the projected values, with a small standard deviation, i.e., less than 3.1 atom % for Pt_2Ru_5 and 1.4 atom % for Pt_3Co. It was also found that these alloys were in a form corresponding to the solid solutions with the fcc structure.

EXPERIMENTAL SECTION

Preparation of Particle-Size-Controlled Carbon-Supported Pt and Pt−M Nanoparticle Catalysts. Figure 1 shows the preparation protocol of Pt and Pt−M (M = Ru and Co) particles highly dispersed on a carbon black support (CB, Ketjen Black EC, specific surface area = 800 $m^2\ g^{-1}$, Lion Co, Ltd.) support. In addition to our conventional nanocapsule method, reported earlier (Scheme 1) (30, 31), we also employed a modified protocol (Scheme 2). The difference between Scheme 1 and Scheme 2 is the timing of the addition of CB to the solution. Both syntheses were performed in a reaction flask (volume = 100 mL) under a N_2 atmosphere with magnetic stirring. First, $Pt(acac)_2$ and metal acetylacetonate, $M(acac)_x$ were dissolved in a mixed solvent of 1,2-hexadecanediol (260 mg) and diphenyl ether (12.5 mL). The projected value of total metal loading on CB was 50 wt % for all samples. The mixture was heated at 110 °C for 20 min in a N_2 atmosphere with magnetic stirring, followed by an addition of a given amount of surfactant (oleic

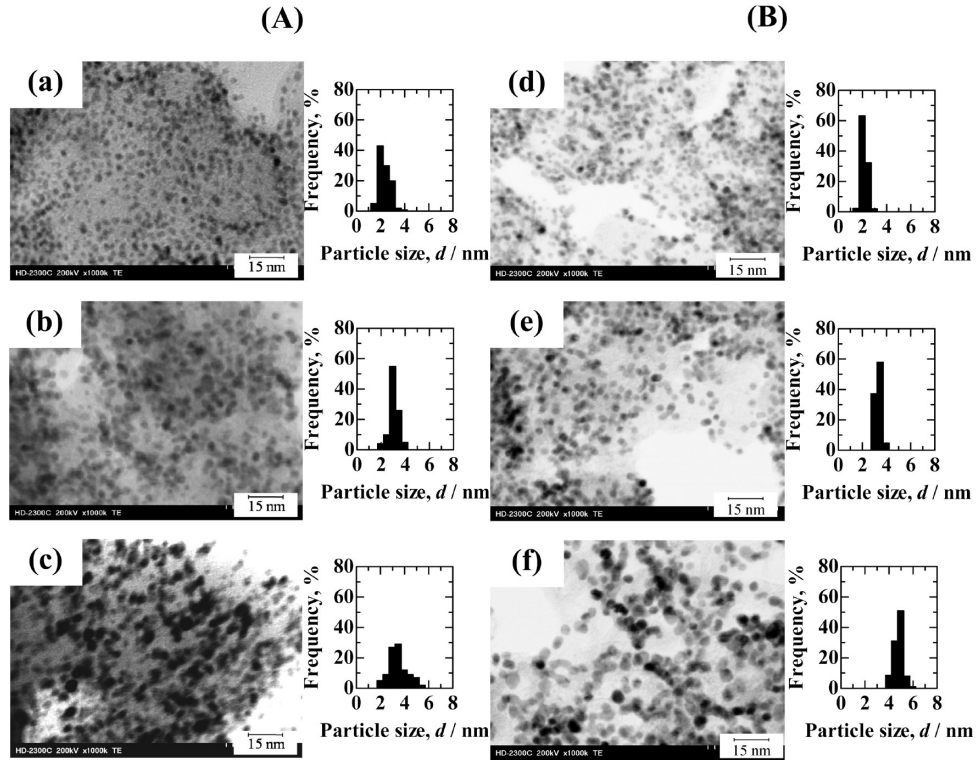

FIGURE 2. STEM images and particle size distribution histograms of Pt/CB catalysts prepared by Scheme 1 (column A) and Scheme 2 (column B) at various M/S ratios: (a, d) M/S = 0.1, (b, e) M/S = 0.5, (c, f) M/S = 1.0. The histograms were obtained among 500 particles in the STEM images.

acid and oleylamine). The molar ratios of metal salt(s) to surfactant (M/S) were adjusted at 0.1, 0.5, and 1.0 in order to control the particle size. CB was then added to the mixed solution in the case of Scheme 1, whereas CB was added after the reduction reaction step in Scheme 2. The temperature was elevated to 220 °C. After maintaining this temperature for 30 min, $LiBEt_3H$ (1.0 mL) was added dropwise into the mixture. The reduction reaction was performed by refluxing the mixture at 270 °C for 30 min. The mixture was then cooled to room temperature. In Scheme 1, the mixture (metal nanoparticles adsorbed on CB with organic moiety) was filtered. In contrast, in Scheme 2, CB was ultrasonically dispersed into diphenyl ether at ca. 30 °C, and the mixture obtained (metal nanoparticles protected by organic nanocapsules) was added dropwise into the CB suspension, followed by elevating the temperature to 270 °C and maintaining that temperature for 30 min. Finally, the mixture was cooled to room temperature and filtered. The powders thus obtained in both Schemes 1 and 2 were dried at 60 °C in a vacuum and were heat-treated at 400 °C for 4 h in flowing N_2 to remove the organic moieties completely.

The catalyst powders thus prepared were characterized by X-ray diffraction (XRD, Rigaku RINT2000) with CuKα radiation (50 kV, 300 mA) and scanning transmission electron microscopy (STEM, Hitachi HD-2300C, acceleration voltage = 200 kV) with an energy-dispersive X-ray analysis (EDX, EDAX Genesis). The loaded amounts of the catalysts on carbon were quantified from the weight loss by combustion of the CB at 600 °C in air.

Electrochemical Measurement. A conventional three-electrode cell was used for all of the electrochemical measurements. Each working electrode consisted of the catalysts uniformly dispersed on a glassy carbon substrate (diameter = 10 mm, geometric area = 0.785 cm^2) at a constant loading of carbon support (5.5 $\mu g\ cm^{-2}$), which corresponds to nominal monolayer height of carbon black particles. Nafion solution (DE521, E.I. du Pont de Nemours & Company Inc.) diluted with ethanol was pipetted on top of the catalyst layer, yielding an average film thickness of 0.05 μm, and was dried under an ethanol-rich atmosphere at room temperature. Finally, the Nafion-coated electrode was heat-treated at 130 °C for 30 min in air. A platinum wire and a reversible hydrogen electrode (RHE) were used as the counter and reference electrodes, respectively. The electrolyte solution of 0.1 M $HClO_4$ was prepared from reagent grade chemicals (Kanto Chemical Co., Japan) and Milli-Q water (Millipore Japan Co., Ltd.) and further purified by conventional pre-electrolysis methods (32, 33).

RESULTS AND DISCUSSION

Characterization of Pt/CB Catalysts Prepared with Various M/S Ratios. Figure 2 shows STEM images of several Pt/CB samples, which were prepared with M/S ratios of 0.1, 0.5, and 1.0 by the two different protocols, Scheme 1 and 2. The particle size distribution histograms among ca. 500 Pt particles are also shown. Typical properties of these catalysts are summarized in Table 1. The platinum metal loading levels in these catalysts prepared by both Scheme 1 and 2 were close to the projected values and nearly independent of the M/S. For the case of Scheme 1, the average particle size (d_{STEM}) and the standard deviations σ_d of the Pt particles prepared at M/S = 0.1, 0.5, and 1.0 were 2.2 ± 0.4, 2.9 ± 0.4, and 3.3 ± 0.8 nm, respectively. The values of d_{STEM} are found to accord well with the crystallite size (d_{XRD}) calculated from Scherrer's equation for the XRD peak assigned to Pt(220). Hence, it is clear that the Pt particle size increased with increasing M/S. However, the σ_d values for the particle size increased abruptly at M/S = 1.0.

When the Pt/CB catalysts were prepared according to Scheme 2, the average Pt particle size also increased with M/S, but the σ_d values remained small, within 0.4 nm (less

Table 1. Typical Properties of Pt/CB Catalysts[a]

catalyst (M/S)	metal loaded[b] (wt %)	d_{XRD}[c] (nm)	d_{STEM}[d] (nm)	ECA[e] (from CV) ($m^2\ g^{-1}$)	SA[f] (from STEM) ($m^2\ g^{-1}$)	lattice constant[g] (pm)
			Scheme 1			
0.1	46.4	1.9	2.2 ± 0.4			392 ± 1
0.5	48.5	2.7	2.9 ± 0.4			393 ± 1
1.0	47.6	2.9	3.3 ± 0.8			393 ± 1
			Scheme 2			
0.1	46.5	2.0	2.0 ± 0.2	115	137	392 ± 1
0.5	48.8	2.9	3.1 ± 0.3	79.4	89.2	393 ± 1
1.0	48.7	4.5	4.5 ± 0.4	64.6	60.9	393 ± 1

[a] Projected loading levels (wt %) of all Pt catalysts were 50 wt %. [b] Metal weight percent in Pt/CB catalysts estimated by weight loss using thermogravimetry (TG). [c] Average crystallite size calculated from Scherrer's equation. [d] Average particle size and the standard deviations σ_d based on the STEM observation. [e] Specific surface area evaluated from the electric charge of hydrogen desorption wave in each CV in Figure 3. [f] Electrochemically active surface area evaluated from STEM images. [g] Average lattice constants and standard deviations.

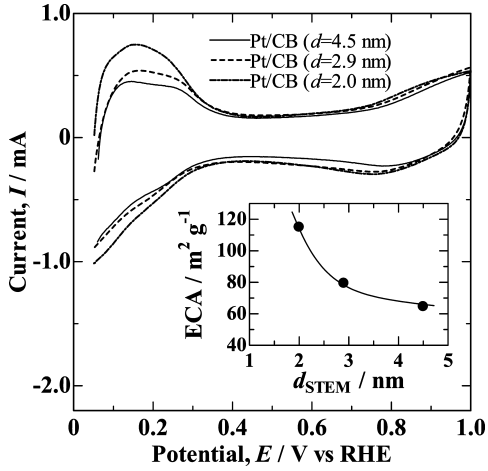

FIGURE 3. Cyclic voltammograms to determine the electrochemically active surface areas, ECA, at a Nafion-coated Pt/CB electrode in 0.1 M $HClO_4$ solution purged with N_2 at 30 °C. Scan rate = 0.1 V s^{-1}.

than 10% of each d_{STEM}), regardless of M/S, i.e., the values of d_{STEM} (with ± σ_d value) were 2.0 ± 0.2, 3.1 ± 0.3, and 4.5 ± 0.4 nm at M/S = 0.1, 0.5, and 1.0, respectively. The d_{STEM} and d_{XRD} values agreed. It is clearly seen in the STEM images that the Pt nanoparticles are uniformly dispersed on the CB support, regardless of the M/S. Thus, by employing Scheme 2 in the preparation, we succeeded in controlling the Pt particle size from 2.0 to 4.5 nm by changing the M/S from 0.1 to 1.0, while maintaining the monodisperse state. It was reported that the size of Pt particles d_{Pt} produced by a method similar to our nanocapsule method corresponded to that of the reverse micelles d_{RM}, as measured by the dynamic light scattering method (34); d_{Pt} was slightly smaller than d_{RM}. It is quite reasonable to consider that d_{RM} can increase with increasing M/S, since the size of the "water pool" containing the metal salts increases when the surfactant concentration is higher than the critical micelle concentration and the reverse micelles are stable in the solvent. The fact that the d_{Pt} values (d_{STEM} and d_{XRD} in Table 1) increased with M/S in both Scheme 1 and Scheme 2 strongly supports such a mechanism for controlling the particle size. However, when CB was mixed during the reduction reaction in Scheme 1, the stability of the reverse micelles may decrease at high M/S ≥ 1.0, probably because of a steric hindrance, which may result in a larger σ value than that observed in Scheme 2.

The electrochemically active surface areas (ECA) of the Pt/CB catalysts prepared by Scheme 2 were examined by cyclic voltammetry. Figure 3 shows typical cyclic voltammograms (CVs) at Nafion-coated Pt/CB in 0.1 M $HClO_4$ solution deaerated with N_2 gas at 30 °C. First, the working electrodes were electrochemically stabilized by potential cycling from 0.05 to 1.0 V at a sweep rate of 0.5 V s^{-1} until a steady-state CV was obtained. The ECA of Pt was calculated from the electrical charge of the hydrogen desorption wave Q_H in each CV obtained by potential sweep from 0.05 to 1.0 at 0.1 V s^{-1}, assuming Q_H^o = 210 μC cm^{-2} for smooth polycrystalline Pt (32, 35). The ECA was found to increase with decreasing Pt particle size. The values of ECA for the Pt/CB catalysts with d_{STEM} = 2.0, 3.1, and 4.5 nm were 115.0, 79.4, and 64.6 $m^2\ g^{-1}$, respectively (see inset of Figure 4), which are close to the specific surface area (SA) calculated from d_{STEM}, assuming a spherical shape for the particles. This indicates that all Pt catalyst surfaces were sufficiently clean to adsorb the expected amounts of hydrogen. Hereinafter, we employed Scheme 2 to prepare various catalysts.

Characterization of Pt-Alloy/CB Catalysts Prepared with Various M/S Ratios. *Pt−Ru/CB Catalysts.* Figure 4 shows the STEM images of Pt_2Ru_3/CB prepared with various M/S values and a commercial Pt_2Ru_3/CB together with the particle size distribution histograms. Typical properties of these catalysts are summarized in Table 2. Nanoparticles were uniformly dispersed on the CB support, and their size distribution histograms were fairly narrow in all of our samples, whereas large particles (>5 nm) were frequently observed in the commercial samples. The average particle sizes d_{STEM} and σ_d values for the catalysts prepared with M/S = 0.3, 0.6, and 1.2 were 2.6 ± 0.2, 3.6 ± 0.3, and 4.5 ± 0.5 nm, respectively; the value of σ_d was less than 10% of each d_{STEM}. The amounts of metal loaded were close to the projected values and nearly independent of the M/S. We examined the alloy composition by EDX spot analysis for 20 randomly selected particles from the STEM observation. Regardless of the M/S values, the average compositions of the catalysts were very close to the projected values (40 atom % Pt and 60 atom % Ru), with a small standard deviation in the composition: σ_{comp} < 2.2−3.1 atom %.

It should be noted that the average particle size itself of the commercial sample, d_{STEM} = 3.5 nm, was close to that of our catalyst at M/S = 0.6, but the standard deviation for the commercial one (σ_d = 0.9 nm) was three times larger than that for our catalyst (σ_d = 0.3 nm). The average alloy composition in the commercial one was also close to the nominal value (given by the manufacturer), but the standard deviation in the composition among particles (σ_{comp} = 5.7 atom %) was larger than that of our catalysts (σ_{comp} = 3.1

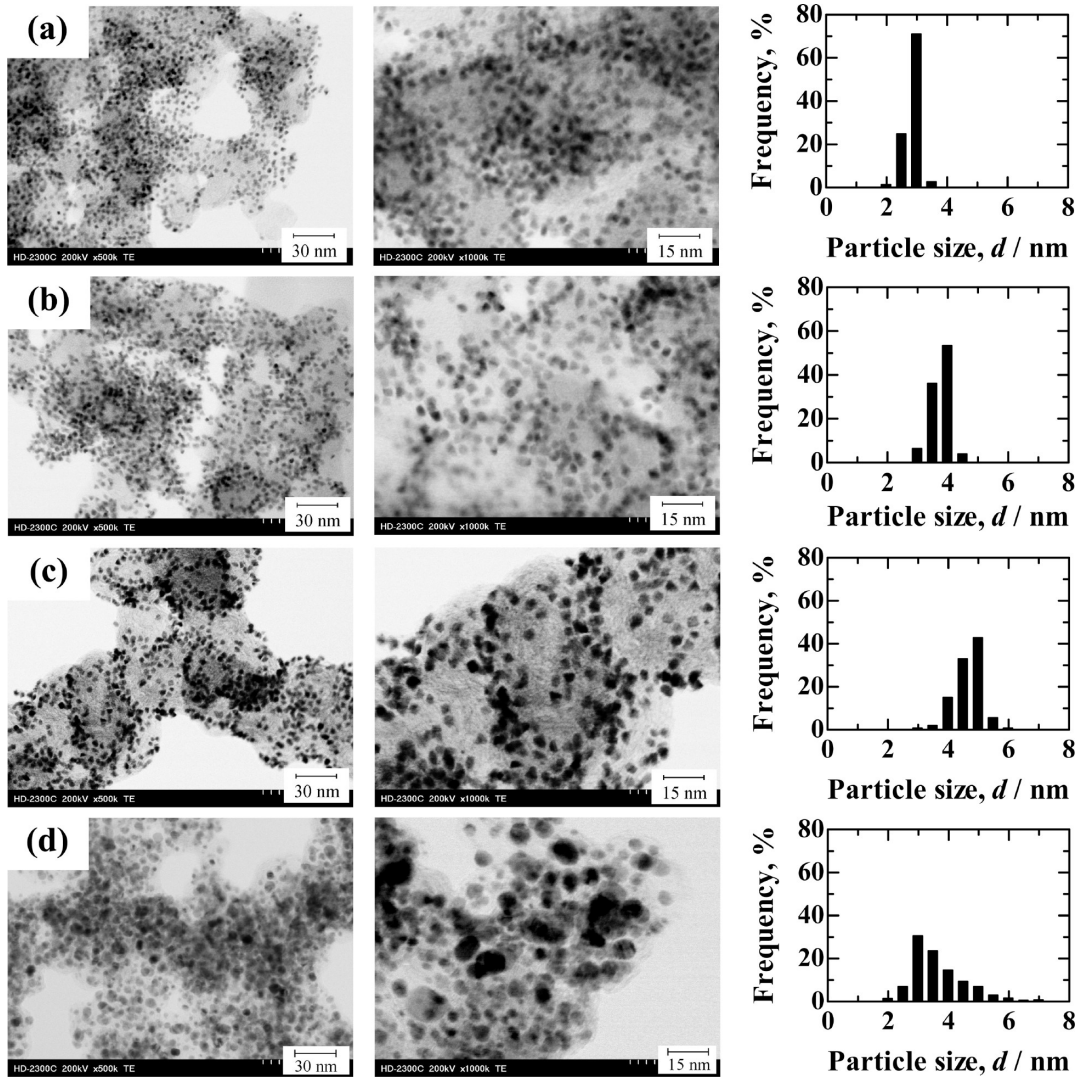

FIGURE 4. STEM images (left column, low-magnification; middle column, high-magnification images) and particle size distribution histograms of Pt_2Ru_3/CB catalysts (right column) prepared with various M/S ratios of (a) M/S = 0.3, (b) M/S = 0.6, and (c) M/S = 1.2, and (d) commercial Pt_2Ru_3/CB catalyst. The histograms were obtained among 500 particles in the STEM images.

Table 2. Typical Properties of Pt_2Ru_3/CB Catalysts[a]

catalyst (M/S)	metal loaded[b] (wt %)	composition[c] Pt (atom %)	composition[c] Ru (atom %)	d_{STEM}[d] (nm)	lattice constant[e] (pm)
0.3	47.4	40.2 ± 2.2	59.8 ± 2.2	2.6 ± 0.2	387 ± 2
0.6	46.4	40.3 ± 3.1	59.7 ± 3.1	3.6 ± 0.3	387 ± 2
1.2	48.6	41.0 ± 2.2	59.0 ± 2.2	4.5 ± 0.5	387 ± 2
commercial	52.9	40.4 ± 5.7	59.6 ± 5.7	3.5 ± 0.9	387 ± 2

[a] Projected loading levels (wt %) of all Pt_2Ru_3 catalysts were 50 wt %. [b] Metal weight percent in Pt_2Ru_3/CB catalysts estimated by weight loss using TG. [c] Average composition and the standard deviations σ_{comp} on the Pt_2Ru_3 particles analyzed by spot-analysis with EDX at 20 particles randomly selected. [d] Average particle size and the standard deviations σ_d based on the STEM observation. [e] Average lattice constants and standard deviations calculated from (111), (200), (220), and (311) diffraction peak in Figure 5.

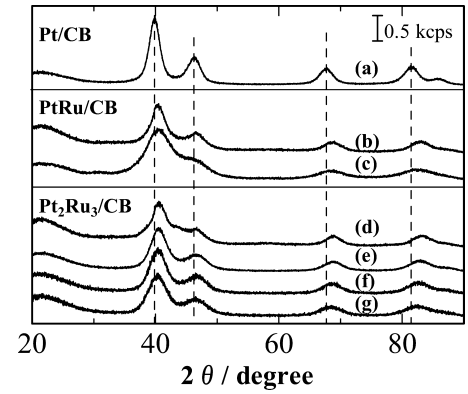

FIGURE 5. X-ray diffraction patterns of (a) Pt/CB (prepared with M/S = 1.0), (b) commercial PtRu/CB, and nanocapsule PtRu/CB prepared with (c) M/S = 0.3. XRD of (d) commercial Pt_2Ru_3/CB, and nanocapsule Pt_2Ru_3/CB prepared with M/S = (e) 1.2, (f) 0.6, and (g) 0.3 are also shown.

atom %). The uniform alloy composition in our nanocapsule catalysts is one of the essential characteristics for the reaction(s) within the nanoscale volume under identical conditions except for the M/S ratio.

Figure 5 shows XRD patterns for various Pt−Ru/CB catalysts, together with Pt/CB (M/S = 1.0). The broad peak at 2θ = ca. 25° for all samples was assigned to amorphous carbon (CB). The diffraction peaks for Pt−Ru/CB were shifted

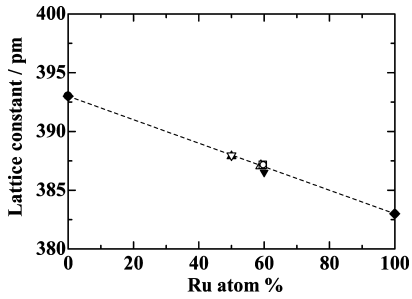

FIGURE 6. Relationship between lattice constant and Ru content (analyzed atomic percent) of Pt_2Ru_3 alloys prepared with (○) M/S = 0.3, (□) M/S = 0.6, and (△) M/S = 1.2. Data for PtRu alloy prepared with (▽) M/S = 0.3 and commercial one are plotted by symbols ▲ and ▼, respectively. Symbols (●) and (♦) indicate the lattice constant of pure Pt and Ru.

to higher angles than the fcc phase of pure Pt. For example, the peak at $2\theta = 39.8°$ is assigned to Pt(111) for Pt/CB, while the corresponding peak for our Pt_2Ru_3 catalysts was observed at ca. 40.4°, irrespective of M/S. No extra peaks assigned to Ru or Ru oxides were identified. The average lattice constant for these Pt−Ru catalysts calculated from (111), (200), (220), and (311) are summarized in Table 2. Figure 6 shows the lattice constant as a function of Ru atom % (analyzed value in Table 2). The average lattice constant of our Pt_2Ru_3/CB and $Pt_{50}Ru_{50}$/CB catalysts (open symbols) and commercial ones (closed symbols) are located on the regression line based on Vegard's law, indicating that the fcc solid solution was formed from Pt and Ru because of the closely matching atomic radii (139 pm for Pt and 134 pm for Ru), even though pure Ru metal belongs to the hexagonal closest packing (hcp) structure. Even though there is a theoretical prediction that ordered Pt−Ru crystal structures exist, e.g., Pt_3Ru and PtRu (36), and experimental evidence for Pt_2Ru_3 (37), it appears that such structures might not lead to a significant difference in lattice constant compared to the corresponding solid solution. Summarizing this section, we have succeeded in controlling the Pt_2Ru_3 alloy particle size from 2.6 to 4.5 nm by changing the M/S ratio from 0.3 to 1.2 while maintaining both the monodisperse state and the uniform alloy composition.

Pt_3Co/CB Catalysts. Figure 7 shows STEM images of the Pt_3Co/CB samples, which were prepared with M/S ratios of 0.3, 0.7, and 1.3, and a commercial Pt_3Co/CB sample, together with the particle size distribution histograms. Typical properties of these catalysts are summarized in Table 3. It is clearly seen for our catalysts in the STEM images that the Pt_3Co nanoparticles are uniformly dispersed on the CB support, and their size distribution histograms are fairly narrow, regardless of M/S. The average particle sizes of these catalysts increased with increasing M/S ratio, i.e., the values of d_{STEM} (with $\pm\sigma_d$ value) were 2.0 ± 0.2 (M/S = 0.3), 2.9 ± 0.3 (M/S = 0.7), and 4.2 ± 0.6 nm (M/S = 1.3). Similar to the cases of Pt/CB and Pt_2Ru_3/CB, d_{STEM} increased with M/S. The metal loading levels were close to the projected value of 50 wt %. The alloy compositions of our catalysts exam-

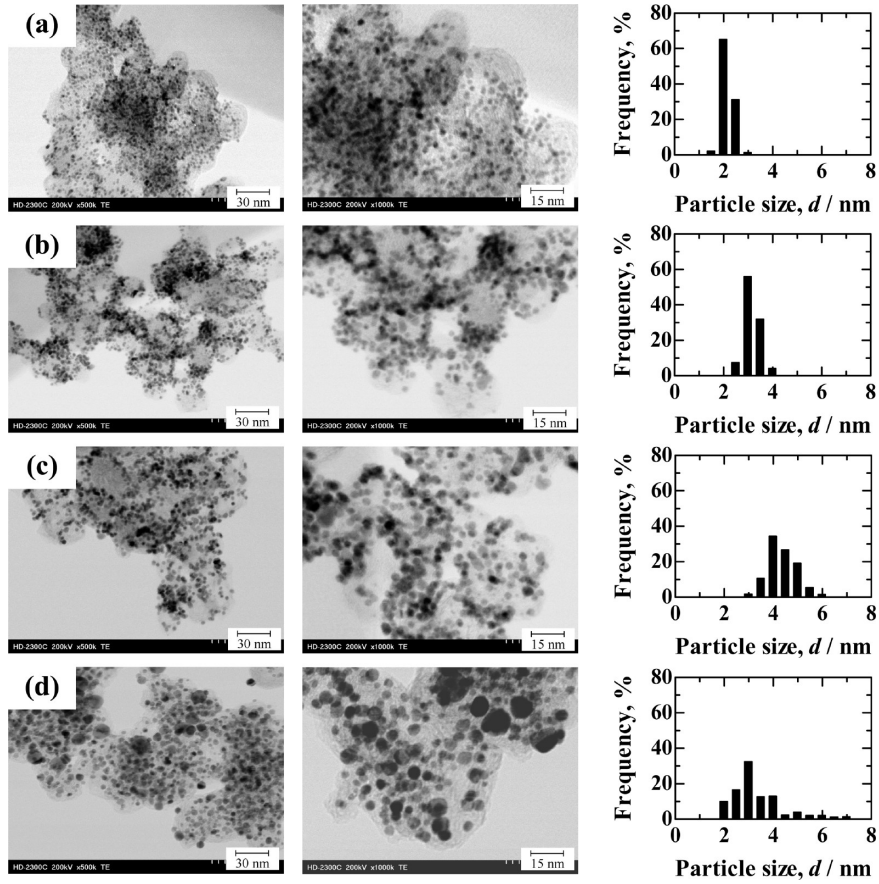

FIGURE 7. STEM images and particle size distribution histograms of Pt_3Co/CB catalysts prepared with various M/S ratios of (a) M/S = 0.3, (b) M/S = 0.7, and (c) M/S = 1.3, and (d) commercial Pt_3Co/CB catalyst. The histograms were obtained among 500 particles in the STEM images.

Table 3. Typical Properties of Pt_3Co/CB Catalysts[a]

catalyst (M/S)	metal loaded[b] (wt %)	composition[c] Pt (atom %)	composition[c] Co (atom %)	d_{STEM}[d] (nm)	lattice constant[e] (pm)
0.3	46.0	74.2 ± 1.4	25.8 ± 1.4	2.0 ± 0.2	387 ± 1
0.7	48.1	76.0 ± 1.3	24.0 ± 1.3	2.9 ± 0.3	385 ± 2
1.3	50.8	76.6 ± 1.2	23.4 ± 1.2	4.2 ± 0.6	386 ± 1
commercial	47.7	75.7 ± 8.2	24.3 ± 8.2	3.3 ± 1.3	385 ± 1

[a] Projected loading levels (wt %) of all Pt_3Co catalysts were 50 wt %. [b] Metal weight percent in Pt_3Co/CB catalysts estimated by weight loss using TG. [c] Average composition and the standard deviation σ_{comp} on the Pt_3Co particles analyzed by spot-analysis with EDX at 20 particles randomly selected. [d] Average particle size and the standard deviations σ_d based on the STEM observation. [e] Average lattice constants and standard deviations calculated from (111), (200), (220), and (311) diffraction peak in Figure 8.

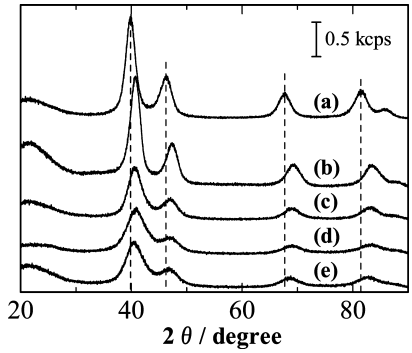

FIGURE 8. X-ray diffraction patterns of Pt_3Co/CB catalysts prepared with (a) Pt/CB catalyst prepared with M/S = 1.0, (b) commercial, (c) M/S = 1.2, (d) M/S = 0.6, and (e) M/S = 0.3.

ined by EDX spot analysis were very close to the projected value of Pt:Co = 3:1, regardless of M/S. The values of σ_{comp} among 20 randomly selected particles were less than 1.5 atom %, whereas that of commercial sample was relatively large: σ_{comp} = 8.2 atom %. Thus, the Pt−Co alloy composition was well controlled in our preparation method. The average particle size itself of the commercial one (d_{STEM} = 3.3 nm) was close to that of our Pt_3Co/CB catalyst prepared at M/S = 0.7, but the σ_d value for the commercial one (σ_d = 1.3 nm) was four times larger than that of our catalyst (σ_d = 0.3 nm).

Figure 8 shows the XRD patterns for our Pt_3Co/CB catalysts, together with that for Pt/CB (M/S = 1.0). The diffraction peaks for Pt_3Co/CB were shifted to slightly higher angles than the fcc phase of pure Pt, without any extra peaks assigned to Co or Co oxides. The average lattice constant for these Pt_3Co catalysts calculated from (111), (200), (220), and (311) in the XRD pattern are summarized in Table 3. Figure 9 shows the lattice constant as a function of Co atom.%. In our previous work (31), we found that the change in the lattice constant of Pt_xCo (x = 1−3) supported on the CB was smaller than that expected from simple Vegard's law, because the atomic radius (125 pm) of pure Co metal (belonging to the hcp structure) is significantly smaller than that of Pt (139 pm) or Ru (134 pm). However, up to 45 atom %, a nearly linear relationship was observed, as shown by the solid line in Figure 9. The average lattice constant of the

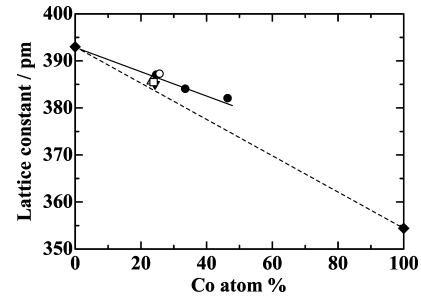

FIGURE 9. Relationship between the lattice constant and Co content (analyzed atomic percent) of Pt_3Co alloys prepared with (○) M/S = 0.3, (□) M/S = 0.7, and (Δ) M/S = 1.3, together with (▼) a commercial one and (♦) pure Pt and Co. Data for Pt_xCo/CB (x = 1, 2, and 3) cited from ref 31 are also shown (●).

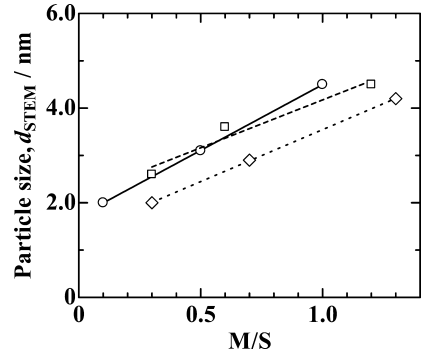

FIGURE 10. Relationship between metal/surfactant mole ratio (M/S) and particle size of (○) Pt, (□)Pt_2Ru_3, and (◇) Pt_3Co (prepared by Scheme 2 in Figure 1).

present Pt_3Co/CB catalysts (open symbols) and commercial Pt_3Co/CB are located on such a regression line. Summarizing this section, we have succeeded in controlling the Pt_3Co alloy particle size from 2.0 to 4.2 nm by changing the M/S from 0.3 to 1.3, while maintaining both the monodisperse state and uniform alloy composition.

Figure 10 shows the average particle size of Pt, Pt_2Ru_3, and Pt_3Co catalysts supported on the CB prepared by Scheme 2. In all samples, the particle size increased nearly in proportion to the M/S value. It is also shown that the particle size of Pt_3Co was somewhat smaller than those of pure Pt and Pt−Ru alloy at a give M/S value, the reason not being clear at the present stage. However, by using these lines as the reference, we can control the particle size with the appropriate M/S for these catalysts. We are performing experiments for the evaluation of the electrochemical activities of these catalysts by using the channel flow double electrode (CFDE) method (27, 30, 31, 38, 39) and attenuated total reflection Fourier transform infrared reflection absorption spectroscopy (ATR-FTIRAS) (40–42).

CONCLUSIONS

We have succeeded in preparing monodisperse Pt, Pt−Ru, and Pt_3Co supported uniformly on carbon black with well-controlled particle size, alloy composition, and loading level with the nanocapsule method. The particle size was well-controlled by changing the molar ratio of metal precursor(s) to surfactant (M/S); the average particle size increased with

increasing M/S while maintaining the standard deviation much smaller than that of the corresponding commercial one.

It was clearly observed that the compositions of the alloy particles were close to the projected values, with very small standard deviations. So far, particle size was controlled by changing the heat-treatment temperature (or time) and/or the metal loading levels on the support. However, this conventional technique resulted in large standard deviations of both particle sizes and compositions. In contrast, in our nanocapsule method, all of the preparation conditions (concentration of metal precursors, heat treatment and metal loading level) were identical, except that the M/S ratio was used to control the particle size. The present research certainly contributes to the development of synthetic methods for electrocatalysts with finely tuned particle size and alloy composition, with which high catalytic activity and durability for PEFCs may be attainable, as well as other applications such as catalysts for various chemical reactions.

Acknowledgment. This work was supported by the funds for "Research on Nanotechnology for High Performance Fuel Cells (HiPer-FC) Project" and "Highly CO-Tolerant Anode Catalysts for Residential PEFCs Project" (for the work on the Pt−Ru/CB anode catalyst) from the New Energy and Industrial Technology Development Organization (NEDO) of Japan.

Supporting Information Available: STEM images and particle size distribution histograms for PtRu catalysts (PDF). This material is available free of charge via the Internet at http://pubs.acs.org.

REFERENCES AND NOTES

(1) Toda, T.; Igarashi, H.; Uchida, H.; Watanabe, M. *J. Electrochem. Soc.* **1999**, *146*, 3750–3756.
(2) Toda, T.; Igarashi, H.; Watanabe, M. *J. Electroanal. Chem.* **1999**, *460*, 258–262.
(3) Toda, T.; Honma, I. *Trans. Mater. Res. Soc. Jpn.* **2003**, *28*, 215–220.
(4) Mukerjee, S.; Srinivasan, S.; Soriaga, M. P.; McBreen, J. *J. Electrochem. Soc.* **1995**, *142*, 1409–1422.
(5) Mukerjee, S.; Srinivasan, S. *J. Electroanal. Chem.* **1993**, *357*, 201–224.
(6) Min, M.; Cho, J.; Cho, K.; Kim, H. *Electrochim. Acta* **2000**, *45*, 4211–4217.
(7) Neergat, N.; Shukla, A. K.; Gandhi, K. S. *J. Appl. Electrochem.* **2001**, *31*, 373–378.
(8) Stamenkovic, V.; Schmidt, T. J.; Markovic, N. M.; Ross, P. N., Jr. *J. Phys. Chem. B* **2002**, *106*, 11970–11979.
(9) Stamenkovic, V.; Schmidt, T. J.; Ross, P. N., Jr.; Markovic, N. M. *J. Electroanal. Chem.* **2003**, *554−555*, 191–199.
(10) Drillet, J.-F.; Ee, A.; Friedemann, J.; Kötz, R.; Schnyder, B.; Schmidt, V. M. *Electrochim. Acta* **2002**, *47*, 1983–1988.
(11) Yang, H.; Vogel, W.; Lamy, C.; Alonso-Vante, N. *J. Phys. Chem.B* **2004**, *108*, 11024–11034.
(12) Paffett, M. T.; Berry, J. G.; Gottesfeld, S. *J. Electrochem. Soc.* **1988**, *135*, 1431–1436.
(13) Thamizhmani, G.; Capuano, G. A. *J. Electrochem. Soc.* **1994**, *141*, 968–975.
(14) Antolini, E.; Passos, R. R.; Ticianelli, E. A. *Electrochim. Acta* **2002**, *48*, 263–270.
(15) Xiong, L.; Manthiram, A. *Electrochim. Acta* **2005**, *50*, 2323–2329.
(16) Paulus, U. A.; Wokaun, A.; Scherer, G. G.; Schmidt, T. J.; Stamenkovic, V.; Radmilovic, V.; Markovic, N. M.; Ross, P. N. *J. Phys. Chem. B* **2002**, *106*, 4181–4191.
(17) Salgado, J. R. C.; Antolini, E.; Gonzalez, E. R. *J. Electrochem. Soc.* **2004**, *151*, A2143–A2149.
(18) Lima, F. H. B.; Ticianelli, E. A. *Electrochim. Acta* **2004**, *49*, 4091–4099.
(19) Beard, B. C.; Ross, P. N. *J. Electrochem. Soc.* **1990**, *137*, 3368–3374.
(20) Shukla, A. K.; Neergat, M.; Bera, P.; Jayaram, V.; Hegde, M. S. *J. Electroanal. Chem.* **2001**, *504*, 111–119.
(21) Arico, A. S.; Poltarzewski, Z.; Kim, H.; Morana, A.; Giordano, N.; Antonucci, V. *J. Power Sources* **1995**, *55*, 159–166.
(22) Luo, J.; Kariuki, N.; Han, L.; Wang, L.; Zhong, C.-J.; He, T. *Electrochim. Acta* **2006**, *51*, 4821–4827.
(23) Freund, A.; Lang, J.; Lehmann, T.; Starz, K. A. *Catal. Today* **1996**, *27*, 279–283.
(24) Ravikumar, M. K.; Shukla, A. K. *J. Electrochem. Soc.* **1996**, *143*, 2601–2606.
(25) Li, W.; Zhou, W.; Li, H.; Zhou, Z.; Zhou, B.; Sun, G.; Xin, Q. *Electrochim. Acta* **2004**, *49*, 1045–1055.
(26) Spinacé, E. V.; Neto, A. O.; Vasconcelos, T. R. R.; Linardi, M. *J. Power Sources* **2004**, *137*, 17–23.
(27) Yano, H.; Inukai, J.; Uchida, H.; Watanabe, M.; Panakkattu, K. B.; Kobayashi, T.; Chung, J. H.; Oldfield, E.; Wieckowski, A. *Phys. Chem. Chem. Phys.* **2006**, *8*, 4932–4939.
(28) Liu, Z.; Ada, E. T.; Shamsuzzoha, M.; Thompson, G. B.; Nikles, D. E. *Chem. Mater.* **2006**, *18*, 4946–4951.
(29) Liu, Z.; Shamsuzzoha, M.; Ada, E. T.; Reichert, W. M.; Nikles, D. E. *J. Power Sources* **2007**, *164*, 472–480.
(30) Yano, H.; Kataoka, M.; Yamashita, H.; Uchida, H.; Watanabe, M. *Langmuir* **2007**, *23*, 6438–6445.
(31) Yano, H.; Song, J. M.; Uchida, H.; Watanabe, M. *J. Phys. Chem. C* **2008**, *112*, 8372–8380.
(32) Watanabe, M.; Motoo, S. *J. Electroanal. Chem.* **1975**, *60*, 259–266.
(33) Uchida, H.; Ikeda, N.; Watanabe, M. *J. Electroanal. Chem.* **1997**, *424*, 5–12.
(34) Chen, D.-H.; Yeh, J.-J.; Huang, T.-C. *J. Colloid Interface Sci.* **1999**, *215*, 159–166.
(35) Watanabe, M.; Motoo, S. *J. Electroanal. Chem.* **1975**, *60*, 267–273.
(36) Curtarolo, S.; Morgan, D.; Ceder, G. *Calphad* **2005**, *29*, 163–211.
(37) Camara, G. A.; Giz, M. J.; Paganin, V. A.; Ticianelli, E. A. *J. Electroanal. Chem.* **2002**, *537*, 21–29.
(38) Yano, H.; Higuchi, E.; Uchida, H.; Watanabe, M. *J. Phys. Chem. B* **2006**, *110*, 16544–16549.
(39) Uchida, H.; Izumi, K.; Aoki, K.; Watanabe, M. *Phys. Chem. Chem. Phys.* **2009**, *11*, 1771–1779.
(40) Watanabe, M.; Sato, T.; Kunimatsu, K.; Uchida, H. *Electrochim. Acta* **2008**, *53*, 6928–6937.
(41) Kunimatsu, K.; Sato, T.; Uchida, H.; Watanabe, M. *Langmuir* **2008**, *24*, 3590–3601.
(42) Sato, T.; Kunimatsu, K.; Uchida, H.; Watanabe, M. *Electrochim. Acta* **2007**, *53*, 1266–1279.

AM9008693